Carbon 137 (2018) 274–281

Contents lists available at ScienceDirect

Carbon

journal homepage: www.elsevier.com/locate/carbon

Scalable cellulose-sponsored functionalized carbon nanorods induced by cobalt for efficient overall water splitting

Ibrahim Saana Amiinu [a], Zonghua Pu [a], Daping He [b], Hellen Gabriela Rivera Monestel [a], Shichun Mu [a, *]

[a] State Key Laboratory of Advanced Technology for Materials Synthesis and Processing, Wuhan University of Technology, Wuhan 430070, PR China
[b] Hubei Engineering Research Center of RF-Microwave Technology and Application, School of Science, Wuhan University of Technology, Wuhan 430070, China

ARTICLE INFO

Article history:
Received 6 February 2018
Received in revised form
2 May 2018
Accepted 12 May 2018
Available online 17 May 2018

Keywords:
Cellulose fibers
Structural evolution
DFT calculations
Overall water splitting
Large scale

ABSTRACT

A balanced design of cheaper, durable, and highly active electrocatalysts for large scale and sustainable hydrogen production is crucial for the emerging hydrogen economy. Herein, a scalable method is implemented to design a very active heteroatom cofunctionalized carbon nanorods with bifunctional electrocatalytic activity via structural transformation of the cellulose fibers from waste tissue paper. Cobalt (Co) is used as both a promoter-catalyst to induce structural evolution of the nanorods, and a self-doped catalyst moiety by coupling with sulfur and nitrogen to enhance the electrocatalytic properties. The obtained catalyst (Co_9S_8@Co-N/C nanorods) displays high hydrogen evolution reaction (HER) and oxygen evolution reaction (OER) activity, resulting in a small overall water splitting potential of 1.61 V@10 mA cm^{-2} and high electrochemical stability for over 70 h. This synthesis approach is further demonstrated to be very suitable for implementation toward large-scale application and can reproduce consistent catalytic properties, which are highly desirable for mass hydrogen production.

1. Introduction

The increasing demand for sustainable green energy has prompted an intense research for eco-friendly, low-cost, and highly efficient energy storage and conversion technologies. Hydrogen evolution reaction (HER) and oxygen evolution reaction (OER) are essential reactions for renewable energy technologies, especially electrolyzers for hydrogen production [1–4]. Hydrogen is regarded as the most promising candidate for fossil fuel replacement in the future [3–5], and the most preferred route to large scale hydrogen production is via water splitting [5,6]. However, the efficiency of water splitting electrolysis is hugely dependent on highly active electrocatalysts. At present, designing economically viable HER/OER electrocatalysts with greatly improved activity and stability still remains a big challenge. Generally, noble-metal-based catalysts particularly Pt and its alloys are the state-of-the-art HER electrocatalysts, while IrO_2 or RuO_2 based materials are efficient for OER. Unfortunately, these materials are very expensive and poorly immune to contamination, as well as lack resilience to endure long-term stability, which seriously hamper their large scale implementation. As an alternative, non-precious metals and metal-free electrocatalysts have been rigorously explored [7,8]. In particular, earth-abundant transition metals have been demonstrated as good candidates for OER and HER. Co-based materials such as spinel Mn-Co oxides [7], cobalt oxide-coated N- and B- codoped graphene hollow spheres [9], cobalt nanoparticles embedded N-doped carbon [10], and $ZnCo_2O_4$ quantum dots [11] have exhibited high catalytic activity toward OER. Likewise, Co@NCN [12], CP/CTs/Co-S [13] and CoNRs/GO-OOH [14] have shown significant catalytic activity toward HER. However, the synthesis routes to these materials are still costly, time-consuming, and often employs toxic and complicated procedures. An emerging subject of great interest to researchers in this field is the conversion of waste materials, particularly waste paper [15–17], biomass [18,19], and plastics [20,21], into functional nanocarbon frameworks such as graphene, carbon nanotubes and water-soluble carbon dots [22,23]. This group of materials has been effectively applied as efficient electrodes for rechargeable batteries [17,24], supercapacitors [25], and electrocatalysis [17,19]. Waste paper and biomass are predominantly cheap, abundant, non-toxic, and easy to process. However,

* Corresponding author.
E-mail address: msc@whut.edu.cn (S. Mu).

https://doi.org/10.1016/j.carbon.2018.05.025
0008-6223/

almost all of the paper or biomass derived carbon frameworks reported only focus on conversion to graphene, carbon nanosheets and carbon nanotubes. Besides, their applications in electrochemical devices are still lacking compared to chemically-derived counterparts. In addition, their conversion to graphene or carbon nanosheets usually requires an activation step by using metal catalysts such as the chemical vapor deposition (CVD) method or by energy intensive KOH activation at very high temperatures (>1000 °C) [18,19]. Such approaches make their synthesis costly and complicated with compromised experimental repeatability, therefore unappealing. Nonetheless, the conversion of waste materials into valuable products for various emerging applications is very attractive from the viewpoint of recycling, environmental-health and cost saving. Therefore, it is essential to develop facile and low-cost techniques for the structural transformation of these waste materials, as well as extensively exploit their benefits for wider electrochemical applications.

In this work, a less complex method is adopted to directly transform the cellulose fibers of waste paper into carbon nanorods co-functionalized with Co, N, and S. Herein, the cellulose fibers serve as a rich carbon template, while Co acts as both a promoter catalyst to induce the structural evolution, and a self-doped active catalytic component by coupling with N and S to boost the catalytic properties. The analysis shows that the resultant catalyst is mainly composed of Co_9S_8 and Co-N integrated carbon nanorod framework (Co_9S_8@Co-N/C). As a catalyst, the Co_9S_8@Co-N/C nanorods exhibit high bifunctional activity and stability toward both HER and OER, leading to a high overall water splitting efficiency.

2. Experimental

2.1. Synthesis of Co_9S_8@Co-N/C nanorods

Typically, 0.92 g of waste tissue paper towel was first purified by soaking in 1.0 M HCl solution.

(20 mL) for 24 h and then thoroughly washed to neutral pH in de-ionized (DI) water, followed by vacuum drying at 80 °C overnight before further use. The purified paper, as carbon template, was then cut into small pieces and added to a cobalt-precursor solution consisting of $Co(NO_3)_2 \cdot 6H_2O$ (0.29 g), $SC(NH_2)_2$ (0.30 g) and NH_4F (0.074 g) in H_2O (70 mL) under constant stirring for 2 h. The mixture was then treated into a sealed Teflon lined autoclave at 180 °C for 24 h without further agitation. The obtained product was thoroughly washed with DI water and dried at 80 °C in vacuum for 24 h. The dried sample was then finally heat treated in a tubular furnace at 800 °C for 4 h under continuous N_2 flow. After naturally cooled to room temperature, the product was again washed to remove impurities and dried at 80 °C for 24 h. The temperature was finally raised to 100 °C for another 2 h before characterization and electrochemical analysis.

2.2. Materials characterization

Transmission electron microscopic (TEM) images were observed using a JEM−2010 FEF high resolution electron microscope at 20 kV. Surface morphologies were observed on a JSM−7100F model field emission scanning electron microscopy (FESEM) at 20 kV. X-ray diffraction (XRD) patterns were acquired on a Rigaku D/MAX-RB diffractometer (Cu-Kα radiation, $\lambda = 1.5406$ Å) at 40 kV. A Lab-RAM Aramis Raman spectrometer was employed for the recording of Raman spectra using Ar-ion laser with an excitation wavelength of $\lambda_{exc} = 632.8$ nm. X-ray photoelectron spectroscopy (XPS) was recorded on a VG Multi-lab 2000 (Al-Kα, E~1486 eV radiation). The content and composition of elements in the sample were also analyzed by using elemental (CHNO) analyzer (Vario EL cube, Germany), and the bulk loading of metallic Co was determined by inductively coupled plasma atomic emission spectroscopy (ICP-AES).

2.3. Electrochemical measurements

The catalyst ink recipe consisting of 5.0 mg of the as-prepared catalyst powder, homogeneously dispersed in a solution of 20 μL Nafion (5 wt %)/480 μL of DI isopropyl alcohol/water/(v/v ~7:3), was mildly sonicated overnight for homogeneity before used. A Hg/HgO electrode was used as a reference electrode and graphite rod (carbon rod: 99.999%, Alfa Aesar) as a counter electrode. The catalyst ink (10 μL) was loaded on a glassy carbon electrode as a working electrode. All measured potentials are referred to the reversible hydrogen electrode (RHE) scale. All electrochemical properties were evaluated in alkaline media (1.0 M KOH solution) at room temperature using a CHI 660E three-electrode workstation. The polarization curves were recorded at the scan rate of 20 mV s^{-1}. All measured polarization curves were corrected for iR losses.

2.4. DFT computations

The plane-wave Density Functional Theory (DFT) calculations were conducted using the CASTEP module (an *Ab Initio* Total Energy Program, Code version: 6546) with the hydrogen binding energy calculated for different active phases. The computation details are given in supplementary information.

3. Results and discussion

3.1. Catalyst structure and composition

Fig. 1a depicts the simplified synthesis route for the preparation of Co_9S_8@Co-N/C nanorod frameworks. The microstructure obtained by FESEM shows that the N, S-codoped carbon (N,S/C-TP) sample without cobalt consists of a stack of uniformly oriented cellulose fiber bundles (Fig. 1b), while that of Co_3O_4 is composed of nanoparticles and randomly mixed with smooth surface nanorods (Fig. S1). However, the reaction of the tissue paper cellulose with the Co-precursors leads to structural transformation of the carbon fiber bundles into integrated carbon nanorods of Co_9S_8@Co-N/C frameworks (Fig. S2). This suggests that Co plays a critical role as a self-promoter catalyst to induce cleavage and separation of the carbon fibers into both stacked (Fig. S3) and free-standing (Fig. 1c) heteroatom-modified carbon nanorod frameworks. It can be presumed that Co induces a breakdown of the cellulose structure and then stimulates self-reorganization of the fragmented carbon atoms together with reactive species of Co, N and S into an integrated nanorod framework.

Different from that of N,S/C-TP (inset of Fig. 1b), Co_3O_4 (Fig. S1a) and Co_9S_8 (Fig. S1b), the nanorod morphology shows fused bead-like features. The EDX elemental mapping (Fig. 1d) clearly confirms the presence and uniform distributions of all elemental species across the nanorod framework. The TEM image (Fig. 1e) also reveals the fused bead-like structure of the nanorods. The selected area HR-TEM images further reveal the crystalline phase of Co_9S_8 (311) with a lattice spacing of ~2.96 Å (**image 1**) and that of Co (111) (inset of Fig. S3b), as well as a typical carbon framework (**image 2**). The fast Fourier transform (FFT) images (inset) indicate that the carbon phase is largely amorphous. As shown in Fig. 2a, the microstructures were further evaluated by powder X-ray diffraction. The diffraction pattern of N,S/C-TP shows a peak at ~23.8° for the (002) diffraction plane of carbon. The new peaks in the diffraction pattern of Co_9S_8@Co-N/C fit well with the diffraction patterns of Co_9S_8 (JCPDS: 03-065-1765) and metallic Co (JCPDS: 03-065-9722)

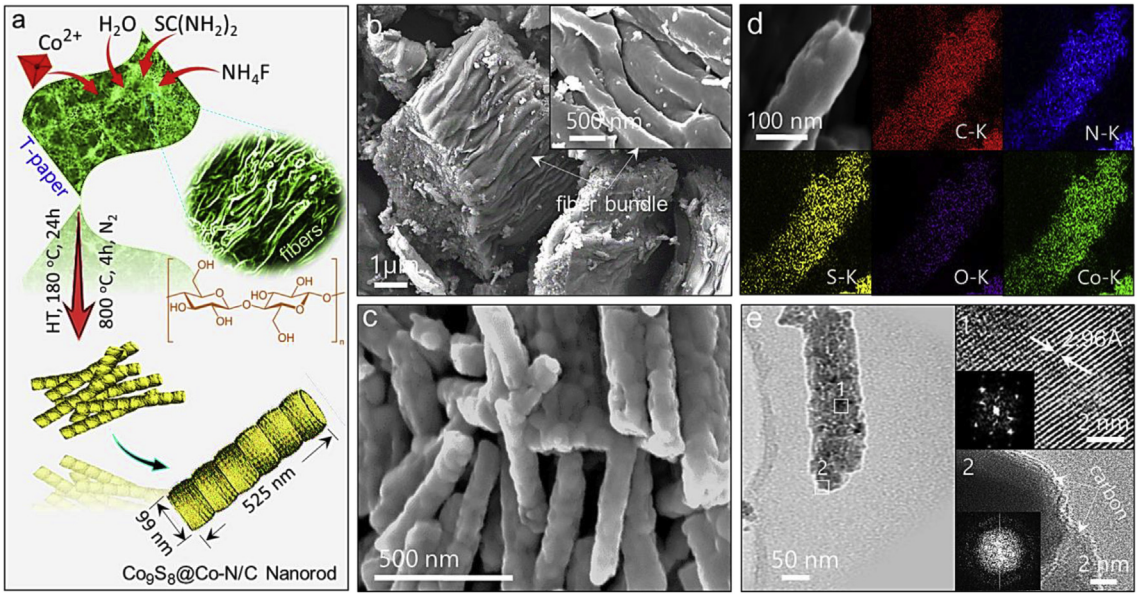

Fig. 1. (a) Synthesis route to the formation of Co_9S_8@Co-N/C nanorods. Inset is the chemical structure of cellulose. FESEM images of (b) N,S/C-TP, (c) Co_9S_8@Co-N/C, (d) EDX elemental mapping of Co_9S_8@Co-N/C. (e) TEM image of a Co_9S_8@Co-N/C nanorod and selected area HR-TEM images (1 and 2) showing lattice fringes of the Co_9S_8 (311) phase and the carbon structure, respectively. Inset is the corresponding fast Fourier transform (FFT) images. (A colour version of this figure can be viewed online.)

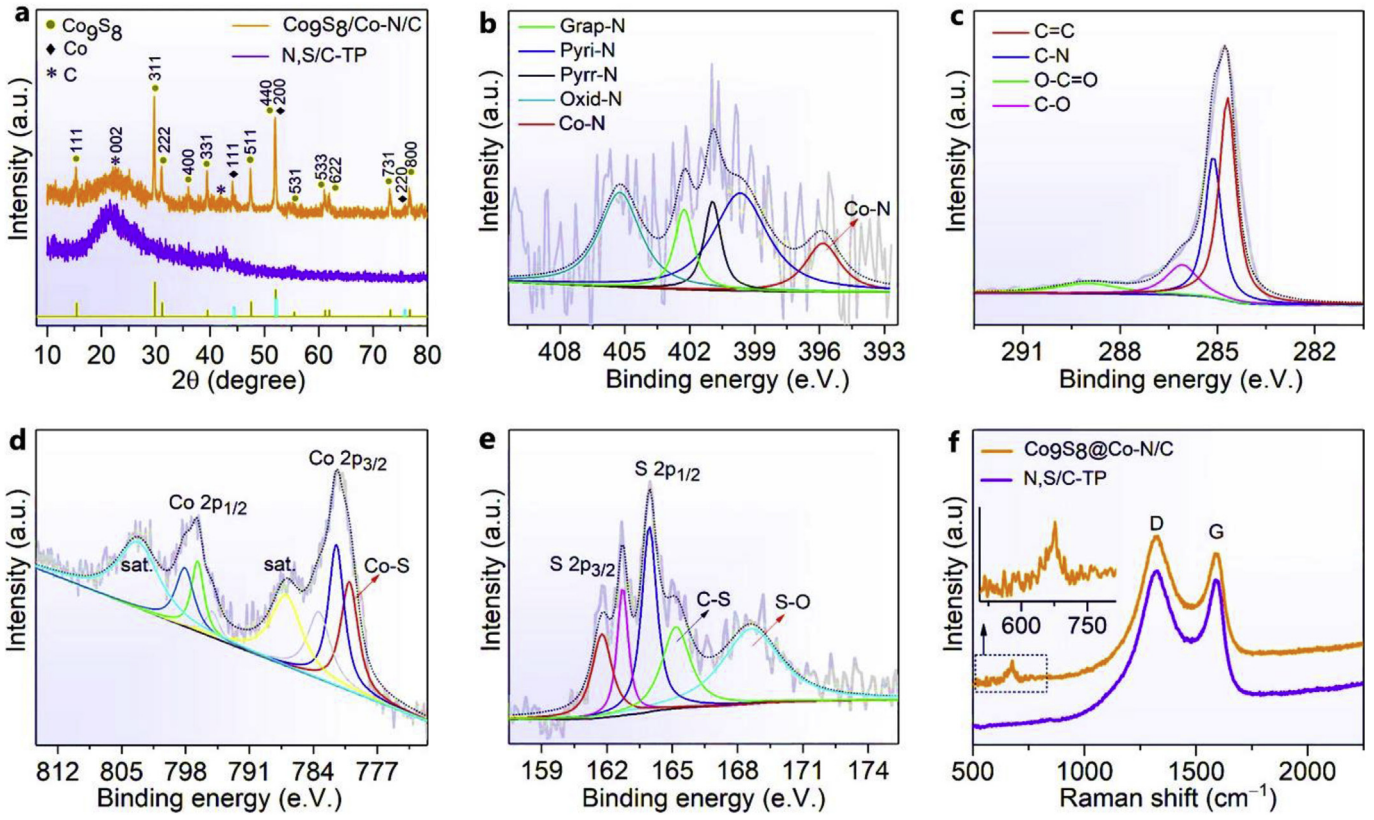

Fig. 2. Microstructure and chemical composition: (a) XRD patterns of Co_9S_8@Co-N/C and N,S/C-TP. High resolution XPS spectra (b) N1s, (c) C 1s, (d) Co 2p (e) S2p of Co_9S_8@Co-N/C. (f) Raman spectra of Co_9S_8@Co-N/C N and S/C-TP. (A colour version of this figure can be viewed online.)

in good agreement with previous literature [26,27]. It is worth nothing that no other phases were observed, indicating that Co_9S_8, metallic Co and carbon are the main phases in the catalyst structure.

The oxidation states and near surface chemical composition of Co_9S_8@Co-N/C were also verified by XPS analysis. The survey scan (Fig. S4) confirms the presence of C, Co, N, S and O species with good atomic concentration of all elements (Table S1). The least-

square fitting of deconvoluted N 1s peaks (Fig. 2c) shows subpeaks of pyridinic (pyri-*N*, ~398.3 eV), graphitic (grap-*N*, ~400.9 eV) and pyrrolic (pyrr-*N*, ~399.3 eV) species. The small peak at ~395.9 eV is attributed to the Co-N bonding phase [26,27]. Pyri-*N* can contribute toward enhancing surface wettability and onset potentials, while grap-*N* contributes to improving the diffusion-limited properties [27–29]. The deconvoluted C 1s peak (Fig. 2c) also shows subpeaks of C–C/C=C (~284.2 eV), C–N (~285.1 eV), O–C (~286.4 eV) and O–C=O (~291.7 eV) species. The detection of C–N phase further confirms the prevalence of N-doped C moieties in the composite carbon framework. The Co $2p_{3/2}$ spectrum (Fig. 2d) presents subpeaks of cobalt sulfide (Co-S, ~780 eV), as well as peaks of surface oxidized Co-species (~781 and~783 eV) and corresponding satellite peaks. Meanwhile, S displays subpeaks of S $2p_{3/2}$ (~162 eV) and S $2p_{1/2}$ (~164.0 eV), as well as peaks of oxidized-S (~169 eV) and sulfhydryl (~163 eV) Fig. 2e. The incorporation of Co and S to form a Co_9S_8 phase is beneficial for molecular adsorption and kinetic reactivity [30,31], while the synergistic effect of Co_9S_8 and Co-N/C frameworks can effectively enhance kinetic activity and overall catalytic performance. The Raman spectrum of N,S/C-TP (Fig. 2f) shows peaks of D- and G-bands (I_D/I_G ratio ~1.05), which are typical features of carbon materials with high defects and low degree of graphitization [32]. The Raman spectrum of Co_9S_8@Co-N/C further displays additional peaks below ~750 cm^{-1} owing to the integrated Co species. The I_D/I_G ratio also slightly increases to ~1.09, indicating higher degree of lattice defects imposed by the doped-Co species and/or by the structural reorganization.

3.2. Theoretical analysis

To further gain detail information on the structure, we probed the electronic-coupling configuration of Co_9S_8@Co-N/C by density functional theory (DFT) computations. The model structures for DFT are shown in Fig. 3a. As displayed in Fig. 3b, Co_9S_8@Co-N/C exhibits a metallic character with no band gap owing to cross over of the Dirac cone. This signals to a charge transfer process from electron-rich regions to electron deficient sites to guarantee uniform charge distribution. This can enhance charge conductivity and benefits the electrocatalytic properties of Co_9S_8@Co-N/C. Furthermore, the projected density of states (DOS) (Fig. 3c) show an overlap of the *s*- and *p*-orbits of Co with that of S, indicating strong covalent interactions between Co and S, as also evidenced by the XPS results. Similarly, the continuity of the *p*-orbit of N reflects the covalent interaction between N and Co atoms of the Co-N coupling phase. Given the importance of HER in the emerging hydrogen economy, we further probed the theoretical activity of Co_9S_8@Co-N/C toward HER. It is well accepted that the Gibbs free energy for hydrogen adsorption ($|\Delta G_{H^*}|$) is strongly correlated to the catalytic activity, and often applied as a key descriptor for forecasting the HER activity of solid electrodes. Therefore, the $|\Delta G_{H^*}|$ was probed for Co_9S_8@Co-N/C and its constituent phases. As displayed in Fig. 3d, the computations suggest that the N,S-codoped-C and Co-N/C have higher $|\Delta G_{H^*}|$ values than Co_9S_8, indicating weak hydrogen binding strength. However, the H*-chemisorption strength must be improved to drag the $|\Delta G_{H^*}|$ value toward zero.

In contrast, coupling the two phases into Co_9S_8@Co-N/C composite structure leads to a significantly lowered $|\Delta G_{H^*}|$ value, suggesting an improved H*-chemisorption properties for efficient HER. Furthermore, the volcano plot of experimentally measured exchange current density (Fig. 3e) reveals that Co_9S_8@Co-N/C is a very competitive HER catalyst compared with common active metallic materials and other active heterostructured electrocatalysts exclusively obtained from toxic chemical reagents. To further gain information on which phase possibly constitutes the most active

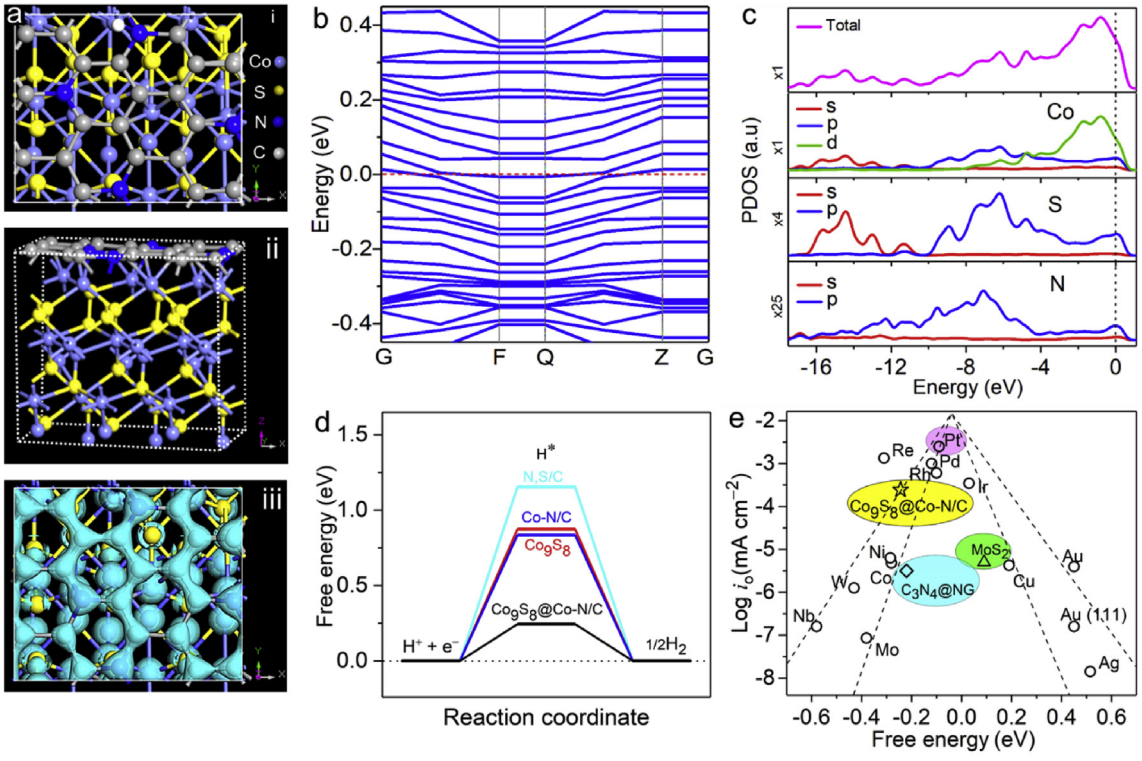

Fig. 3. (a) Atomic structural model of Co_9S_8@Co-N/C; (i) Top-view (ii) side-view (iii) Spatial-distributions of electron density (acqua color; the isovalue is 1.15 a.u). (b) Band structure of Co_9S_8@Co-N/C (c) Calculated total and partial density of states of Co_9S_8@Co-N/C. Dash lines represents the Fermi level. (d) The calculated free-energy diagram of the catalysts. (e) The volcano plot of experimentally measured exchange current density of Co_9S_8@Co-N/C in comparison with various active metal catalysts. Data are drafted from Ref. [33]. (A colour version of this figure can be viewed online.)

site, the partial DOS of the Co-3d orbital was evaluated in accordance with the *d*-band theory, whereby hybridization of chemisorbed H*-orbital with the *d*-orbital of metals can lead to lower energies for filled bonding sates [34]. Accordingly, the activation barrier for bond breaking is the lowest when the *d*-band center is at the Fermi level [34,35]. As shown in Fig. S5, the highest peak of active center DOS is in the order of Co-N/C < Co_9S_8 < Co_9S_8@Co-N/C toward the Fermi level, suggesting that the H*-chemisorption on the composite catalyst surface is slightly more favorable on the Co_9S_8 site. Consequently, the synergistic effect of Co_9S_8 with the active centers of Co-N/C phase significantly boosts the HER activity of Co_9S_8@Co-N/C.

3.3. Electrocatalytic performance of the catalysts

3.3.1. HER activity and stability

On the basis of the theoretical forecasts, the catalytic activity of Co_9S_8@Co-N/C toward HER was experimentally evaluated. First, the electrocatalytic activity and stability toward HER were probed by linear sweep voltammetry at room temperature in 1.0 M KOH solution. As shown in Fig. 4a, Co_9S_8@Co-N/C displays an impressive HER activity, attaining the geometric current density of 10 mA cm^{-2} at an overpotential of η~152 mV versus RHE. This value is much lower than that of N,S/C-PT (η~459 mV), Co_9S_8 NPs (η~362 mV), and Co_3O_4 NPs (η~678 mV); and even lower than most recently reported transition-metal based electrocatalysts including Co_9S_8@NPC-10 (η~261 mV) [36], Co_9S_8@C (η~250 mV) [37], Co-CoO/N-rGO (η~310 mV) [38], MoS_2/Mo (η~172 mV) [39], CP/CTs/Co-S (η~190 mV) [13], MoS_x/CNTs aerogel (η~205 mV) [40] and Mo_2C-R (η~200 mV) [41], as well as many other similar materials (Table S2). Moreover, Co_9S_8@Co-N/C presents a Tafel slope of ~78 mV/dec (Fig. 4b) and a high corresponding exchange current density (i_o) of ~2.45×10^{-4} A cm^{-2} (Fig. S6). The high catalytic activity of Co_9S_8@Co-N/C can be attributed to synergistic effect of the Co_9S_8 and Co-N/C coupling phases. Especially, the N-dopants within Co-N/C fragments could enhance the charge density distribution to benefit the HER activity. It has been previously demonstrated that the inevitable surface oxidation of Co generates active species which can effectively contribute to catalytic activity [42]. Another contributing factor is the free-standing morphology of the nanorods which is favorable for exposing more active sites, as well as free-flow diffusion and rapid mass transport of reactants [43]. These are necessary for enhancing catalytic activity and stability. The uniform distribution of chemical phases, as indicated by XPS and EDX mapping, can also ensure uniform kinetic activity across the nanorod framework and benefit the catalytic performance. As an important requirement for viable and sustainable hydrogen production, the electrochemical stability of Co_9S_8@Co-N/C was also investigated via an accelerated degradation test by cycling under static conditions. As shown in Fig. 4c, Co_9S_8@Co-N/C sustains the current density of 10 mA cm^{-2} with negligible degradation of the overpotential after 2000 potential cycles. This high stability is further corroborated by the time-dependent analysis of the current density (inset of Fig. 4c), which also shows that Co_9S_8@Co-N/C has only a negligible degradation of current density even after 20 h. The slight degradation of the stability can be attributed to gradual oxidation of the electrode and/or loss of activity possibly due to minor leaching of Co-species.

3.3.2. OER activity and stability

Given the high HER performance, the OER activity was also probed in the more positive potential region as shown in Fig. 4d. Interestingly, Co_9S_8@Co-N/C also displays a considerably high onset potential and requires an overpotential as small as ~373 mV to achieve the current density of 10 mA cm^{-2}, approaching that of the benchmark IrO_2 catalyst and far superior to N,S/C-TP, Co_9S_8 NPs, and Co_3O_4 NPs. This notable OER performance is even far superior to similar active electrocatalysts reported recently, including Co@Co_3O_4/NC-1 (η~420 mV) [44], Co_3O_4/NBGHSs (η~470 mV) [9], and Fe/N/C@BMZIF (η~430 mV) [45], which were completely derived from toxic chemical reagents through complex procedures. The Co_9S_8@Co-N/C catalyst also presents a low Tafel slope of ~82.9

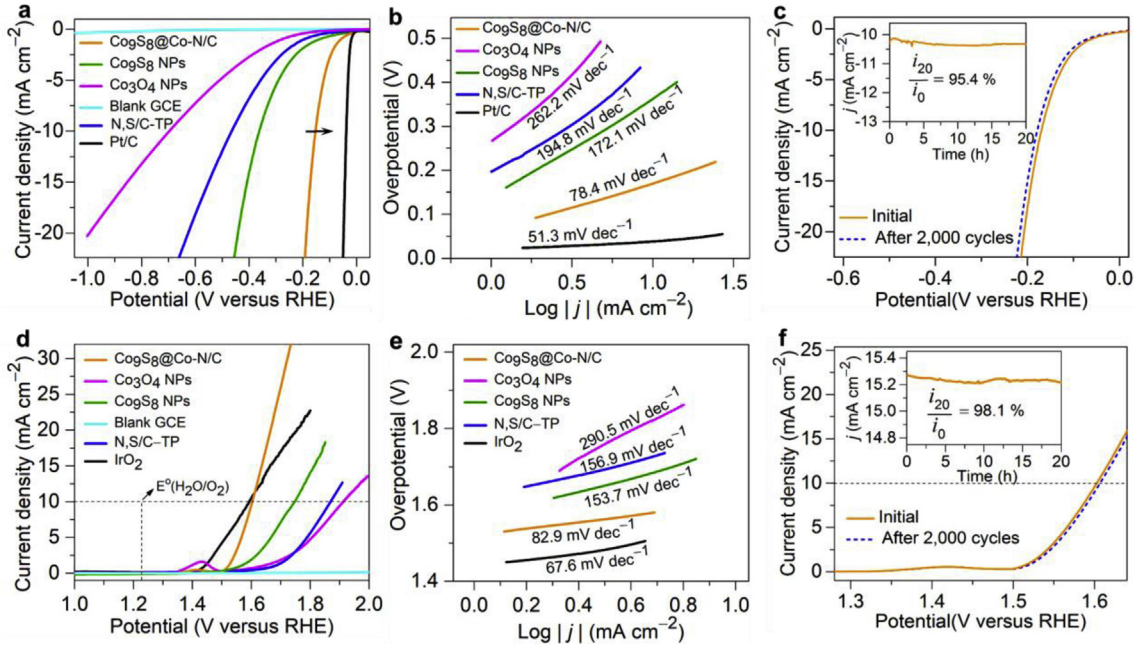

Fig. 4. HER and OER performance of Co_9S_8@Co-N/C in comparison with other catalysts. (a, d) Polarization curves (b, e) Tafel plots, (c, f) Polarization curves recorded for Co_9S_8@Co-N/C before and after 2000 accelerated potential sweeps, respectively, insert figures in c and f are the corresponding chronoamperometric response of current density stability under constant overpotential of 270 mV (HER) and 300 mV (OER) for 20 h, respectively. (A colour version of this figure can be viewed online.)

mV/dec^{-1} (Fig. 4e) approaching that of IrO_2 (~67.6 mV/dec^{-1}). Furthermore, Co_9S_8@Co-N/C is very stable toward OER and keeps high stability without significant degradation even after 2000 accelerated CV cycles (Fig. 4f). A further scrutiny of the OER stability by chronoamperometric response at a constant applied overpotential of 300 mV (inset of Fig. 4f), shows that Co_9S_8@Co-N/C can sustain the current density without any significant degradation even after 20 h. The high OER activity of Co_9S_8@Co-N/C is possibly due to boosted adsorption of OH^- and improved transport of intermediate oxygen-containing products such as superoxides and peroxides. In addition, the high electronegativity of oxygen than carbon, coupled with the high electron affinity of doped-N, could introduce more positively charged neighboring carbon atoms as OER active site. Besides, heteroatoms (N, S) bonded Co frameworks are well-known state-of-the-art active OER catalyst [32,42,44]. This implies that the presence of Co-N and Co-S coupling centers in the nanorod framework can greatly benefit the OER activity. However, in the strongly oxidative OER environment, the Co_9S_8 phase can easily undergo oxidation to form surface oxides or hydroxides owing to the less thermodynamic stability of metal-sulfides [46,47]. Such formed surface oxides or hydroxides can act as active catalytic species and contribute to the high OER performance of the catalyst [46]. Furthermore, Co_9S_8@Co-N/C displays a high Co^{2+} to Co^{3+} ratio of ~0.92, even higher than that of Fe_1Co_1-ONS (~0.89) and Fe_1Co_1-ONP (~0.50), indicating the presence of oxygen vacancies and high favorability toward OER [42].

3.3.3. Water splitting performance

Based on the impressive HER and OER activity, the catalysts were further evaluated for overall water splitting reactions. During electrochemical water splitting, H_2 is generated at the cathode side while O_2 is produced at the anode owing to the transfer of electrons from the anode to cathode. Herein, both electrodes were coated with either Co_9S_8@Co-N/C or Pt/C-IrO_2 catalyst. As shown in Fig. 5a, Co_9S_8@Co-N/C (HER) || Co_9S_8@Co-N/C (OER) couple effectively delivers an overall water splitting current density of 10 mA cm^{-2} at a potential as low as 1.61V in 1.0 M KOH solution. This potential is almost equivalent to that of the costly benchmark catalysts (~1.60 V for Pt/C + IrO2 in this work, and ~1.59 V for Pt/C + RuO2 in Ref. [48]), and comparatively lower than recently reported transition-metal based catalysts (inset of Fig. 5a) including CP/CTs/Co-S (1.74 V) [13], Co-doped $NiSe_2$ (1.62 V) [48] and PBAs@PANI (1.71 V) [49]. The effectiveness of Co_9S_8@Co-N/C toward overall water splitting is demonstrated by the intense gas bubbles evolving from both electrodes as shown in Figs. 5b and Fig. S5. See Video 1 in supporting information for the real time demonstration. The efficiency of the catalysts for water splitting electrolysis is further illustrated in Fig. 5c, whereby the Co_9S_8@Co-N/C|| Co_9S_8@Co-N/C couple exhibits high durability for over 70 h without significant degradation compared to the benchmark Pt/C + IrO_2 catalyst. This demonstrates the high potentials of Co_9S_8@Co-N/C nanorods for design of practicable and cheap water splitting electrolyzers.

Supplementary video related to this article can be found at https://doi.org/10.1016/j.carbon.2018.05.025.

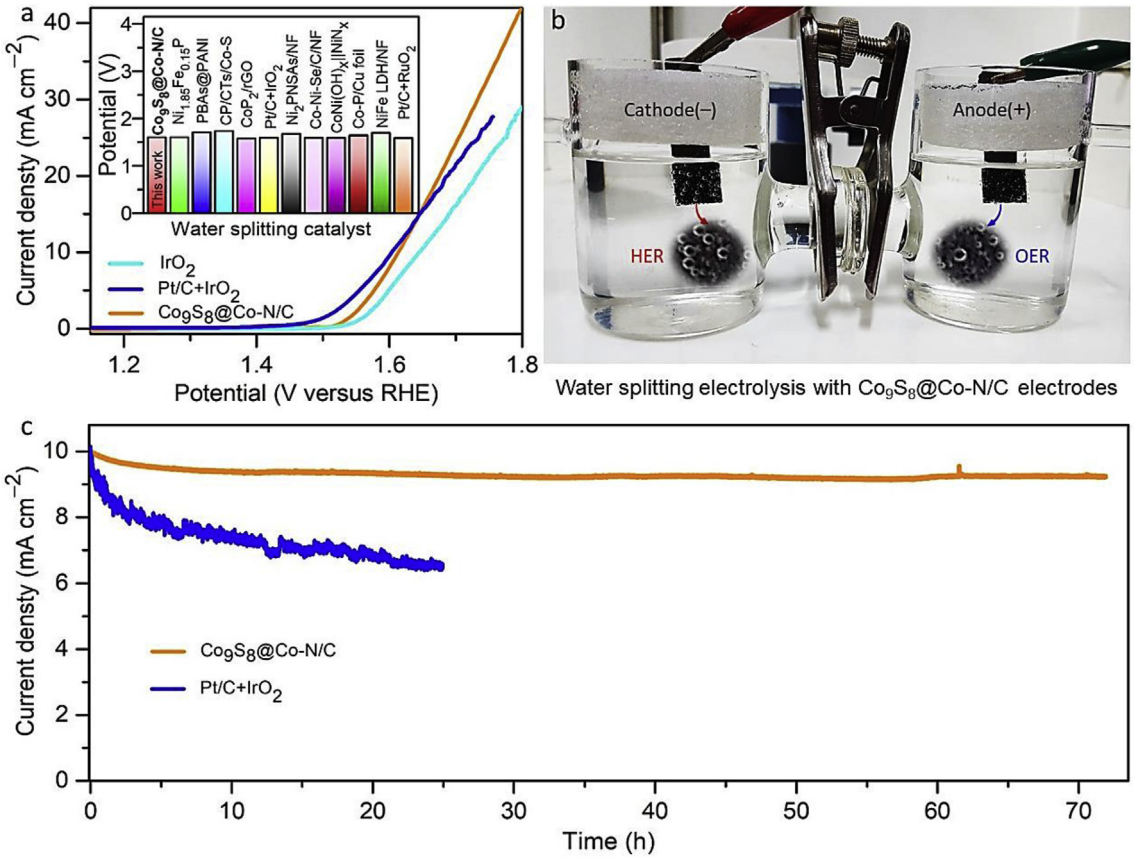

Fig. 5. Overall water splitting performance of Co_9S_8@Co-N/C couple and Pt/C + IrO_2 couple in 1.0 M KOH solution: (a) Polarization curves. Inset is the comparison of water splitting potential of Co_9S_8@Co-N/C with recently reported highly active catalysts. Data are collected from references displayed in supporting information. (b) Setup for the water splitting experiment with Co_9S_8@Co-N/C coated carbon paper electrode (1.0 cm^{-2}) in separate compartments. The bubbles represent the gas evolution. See video 1 in supporting information for demonstration. (c) Electrochemical stability of Co_9S_8@Co-N/C || Co9S8@Co-N/C in comparison with Pt/C + RuO_2 || Pt/C + RuO_2 couple electrodes for overall water splitting. (A colour version of this figure can be viewed online.)

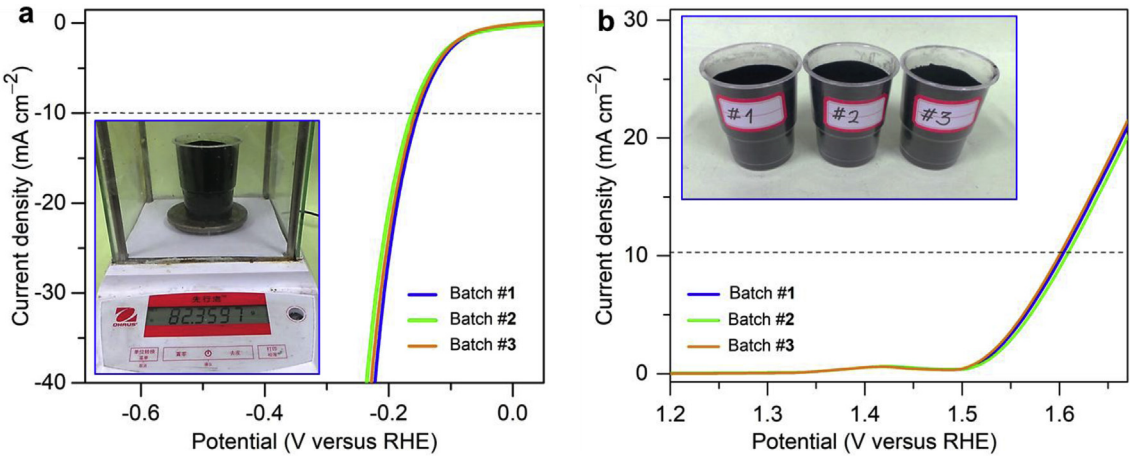

Fig. 6. (a) HER and (b) OER polarization curves of Co_9S_8@Co-N/C produced in three batches by large-scale synthesis approach. The inset in Fig. a and b are photographic images showing the amount in mass (~82.4 g) and volume of samples from the three batches, respectively. (A colour version of this figure can be viewed online.)

The effects of the electrochemical water splitting reactions on the crystalline structure, chemical phases, and morphology were also probed after use of the catalyst for over 25 h. As shown in the XRD patterns (Fig. S8), no significant effects on the crystalline structure can be observed, indicative of high structural stability. Moreover, the FESEM and HR-TEM images (Figs. S9a and b) shows that the morphological features are well-reserved except the slight increase of surfaces roughness of the nanorods. This can be attributed to electrochemical reaction/electrolyte induced oxidation of surface species and/or minor effects due to minimal leaching away of cobalt species. The phenomenon of surface oxidation is confirmed by the XPS and HR-TEM (Fig. S10c) analysis of the catalyst after the electrochemical reaction. The survey scan shows an increase of oxygen content (Fig. S10a, Table S1), while the Co $2p_{3/2}$ peak also slightly shifts upward (Fig. S10b). All of these observations are manifestation of surface oxidation.

3.3.4. *Scalable production and catalytic performance*

A key motivation for the study of non-noble materials is their high potential for cost-effective mass production and large-scale application in electrochemical devices. Undoubtedly, one serious drawback to large-scale implementation of non-noble catalytic materials is that most active catalysts are only confined to lab-scale synthesis with limited prospects for real scalability and practical applications. Such constraints are mainly related to complex synthesis routes, toxicity of chemical reagents, and time-consuming procedures. Herein, given the abundance and low cost of such waste papers, we further exploited the benefits of value-addition by evaluating the suitability of our method for mass production. To this end, a scale-up procedure was implemented toward a relatively large-scale synthesis of Co_9S_8@Co-N/C nanorods catalyst (Fig. S11). As shown in the inset of Fig. 6a, a typical amount of ~82.4 g of catalyst sample was repeatedly reproduced in three batches (~247.2 g) (Fig. 6b inset), demonstrating high prospects for large-scale production. As a model procedure, catalyst samples from all three batches were also probed for consistency of their catalytic properties. In this regard, the catalyst ink was formulated with samples from each batch and electrochemically evaluated for both HER and OER as displayed in Fig. 6a and b, respectively. Interestingly, all three batches exhibit almost equivalent catalytic activity and high reproducibility, demonstrating that our synthesis method is very reliable for replicating consistent electrochemical properties even by large scale production. Furthermore, all three batches display similar HER overpotentials under potential cycling without significant degradation even after 5000 cycles (Fig. S12).

4. Conclusion

In summary, we have successfully applied cobalt as a self-promoter catalyst to induce the structural transformation of the cellulose fibers of waste tissue paper into free-standing Co, N and S co-functionalized Co_9S_8@Co-N/C nanorods with a uniform distribution of all chemical components. Benefiting from the synergistic chemical composition of active Co_9S_8 and Co-N coupling phases within the nanorod framework, the catalyst exhibits high catalytic activity and excellent stability toward both HER and OER, resulting in efficient overall water splitting at a small potential of 1.61 V. The free-standing nanorod structure also benefits the catalytic activity by improving diffusion and mass transport efficiency. All three batches, produced by a relatively large-scale approach, show equivalent catalytic activity without any significant disparities, indicating good reliability to replicate consistent electrochemical properties. This demonstrates that our approach is suitable and can be applied to prepare cheap and scalable bifunctional electrocatalysts from waste tissue paper. The low cost, high prospects for scalability, and robust performances make Co_9S_8@Co-N/C a potential bifunctional catalyst for application in large-scale hydrogen production, and could be exploited for other electrochemical energy devices.

Acknowledgements

This work was financed by the Natural Science Foundation of China (Grant No.: 51372186 and 51672204). The authors express thanks to Xiaoqing Liu and Tingting Luo in the Materials Analysis Center of Wuhan University of Technology for TEM measurements. The authors also wish to sincerely acknowledge the anonymous reviewers for their constructive review remarks and valuable suggestions.

Appendix A. Supplementary data

Supplementary data related to this article can be found at https://doi.org/10.1016/j.carbon.2018.05.025.

References

[1] J.A. Turner, Science 305 (2004) 972–974.
[2] I.S. Amiinu, Z. Pu, X. Liu, K.A. Owusu, H.G.R. Monestel, F.O. Boakye, H. Zhang, S. Mu, Adv. Funct. Mater. 27 (2017) 1702300.
[3] S. Jinga, L. Zhang, L. Luob, J. Lub, S. Yinb, P.K. Shenb, P. Tsiakaras, Appl. Catal. B Environ. 224 (2018) 533–540.
[4] M.S. Dresselhaus, I.L. Thomas, Nature 414 (2001) 33–34.
[5] M.T.M. Koper, E. Bouwman, Angew. Chem. Int. Ed. 49 (2010) 3723–3725.
[6] D.G. Nocera, Acc. Chem. Res. 45 (2012) 767–776.
[7] A. Zhao, J. Masa, W. Xia, A. Maljusch, M.G. Willinger, G. Clavel, X. Kunpeng, R. Schlög, W. Schuhmann, M. Muhler, J. Am. Chem. Soc. 136 (2014) 7551–7554.
[8] I.S. Amiinu, J. Zhang, Z. Kou, X. Liu, K.A. Owusu, H. Zhou, C. Kun, H. Zhang, L. Mai, M. Pan, S. Mu, ACS Appl. Mater. Interfaces 8 (2016) 29408–29418.
[9] Z. Jiang, Z.J. Jiang, T. Maiyalagan, A. Manthiram, J. Mater. Chem. A. 4 (2016) 5877–5889.
[10] Y. Su, Y. Zhu, H. Jiang, J. Shen, X. Yang, W. Zou, J. Chen, C. Li, Nanoscale 6 (2014) 15080–15089.
[11] Z.Q. Liu, H. Cheng, N. Li, T.Y. Ma, Y.Z. Su, Adv. Mater. 28 (2016) 3777–3784.
[12] X. Dai, Z. Li, Y. Ma, M. Liu, K. Du, H. Su, H. Zhuo, L. Yu, H. Sun, X. Zhang, ACS Appl. Mater. Interfaces 8 (2016) 6439–6448.
[13] J. Wang, H.X. Zhong, Z.L. Wang, F.L. Meng, X.B. Zhang, ACS Nano 10 (2016) 2342–2348.
[14] B. Tian, W. Zhen, H. Gao, X. Zhang, Z. Li, G. Lu, Appl. Catal. B Environ. 203 (2017) 789–797.
[15] K.H. Adolfsson, S. Hassanzadeh, M. Hakkarainen, RSC Adv. 5 (2015) 26550–26558.
[16] T.N. Ye, W.J. Feng, B. Zhang, M. Xu, L.B. Lv, J. Su, X. Wei, K.X. Wang, X.H. Li, J.S. Chen, J. Mater. Chem. 3 (2015) 13926–13932.
[17] C.H. Chang, S.H. Chung, A. Manthiram, Sustain. Energy Fuels 1 (2017) 444–449.
[18] A. Primo, P. Atienzar, E. Sanchez, J.M. Delgado, H. García, Chem. Commun. 48 (2012) 9254–9256.
[19] H. Zhou, J. Zhang, I.S. Amiinu, C. Zhang, X. Liu, W. Tu, M. Pan, S. Mu, Phys. Chem. Chem. Phys. 18 (2016) 10392–10399.
[20] G. Ruan, Z. Sun, Z. Peng, J.M. Tour, ACS Nano 5 (2011) 7601–7607.
[21] J. Deng, Y. You, V. Sahajwalla, R.K. Joshi, Carbon 96 (2016) 105–115.
[22] A. Suriani, A.R. Dalila, A. Mohamed, M.H. Mamat, M. Salina, M.S. Rosmi, J. Rosly, R.M. Nor, M. Rusop, Mater. Lett. 101 (2013) 61–64.
[23] J. Wei, J. Shen, X. Zhang, S. Guo, J. Pan, X. Hou, H. Zhang, L. Wang, B. Feng, RSC Adv. 3 (2013) 13119–13122.
[24] X. Xie, T. Makaryan, M. Zhao, K.L.V. Aken, Y. Gogotsi, G. Wang, Adv. Energy Mater. (2015), 1502161.
[25] L. Sun, L. Sun, C. Tian, M. Li, X. Meng, L. Wang, R. Wang, J. Yin, H. Fu, J. Mater. Chem. 1 (2013) 6462–6470.
[26] X. Liu, I.S. Amiinu, S. Liu, K. Cheng, S. Mu, Nanoscale 8 (2016) 13311–13320.
[27] I.S. Amiinu, X. Liu, Z. Pu, W. Li, Q. Li, J. Zhang, H. Tang, H. Zhang, S. Mu, Adv. Funct. Mater. 28 (2017) 1704638.
[28] D. Yu, K. Goh, H. Wang, L. Wei, W. Jiang, Q. Zhang, L. Dai, Y. Chen, Nat. Nanotechnol. 7 (2014) 555–562.
[29] D. Guo, R. Shibuya, C. Akiba, S. Saji, T. Kondo, J. Nakamura, Science 351 (2016) 361–562.
[30] T. Liu, L. Zhang, Y. Tian, J. Mater. Chem. 6 (2018) 5935–5943.
[31] S. Huang, Y. Meng, S. He, A. Goswami, Q. Wu, J. Li, S. Tong, T. Asefa, M. Wu, Adv. Funct. Mater. 27 (2017) 1606585.
[32] F. Zheng, Y. Yang, Q. Chen, Nat. Commun. 5 (2014) 5261.
[33] Y. Zheng, Y. Jiao, Y. Zhu, L.H. Li, Y. Han, Y. Chen, A. Du, M. Jaroniec, S.Z. Qiao, Nat. Commun. 5 (2014) 3783.
[34] E. Santos, W. Schmickler, ChemPhysChem 7 (2006) 2282–2285.
[35] B. Hammer, J.K. Nørskov, Nature 376 (1995) 238–240.
[36] R. Li, H. Zhang, X. Zhang, T. Wu, H. Zhao, G. Wang, RSC Adv. 7 (2017) 19181–19188.
[37] L.-L. Feng, G.-D. Li, Y. Liu, Y. Wu, H. Chen, Y. Wang, Y.-C. Zou, D. Wang, X. Zou, ACS Appl. Mater. Interfaces 7 (2015) 980–988.
[38] X. Liu, W. Liu, M. Ko, M. Park, M.G. Kim, P. Oh, S. Chae, S. Park, A. Casimir, G. Wu, J. Cho, Adv. Funct. Mater. 25 (2015) 5799–5808.
[39] Z. Pu, Q. Liu, A.M. Asiri, Y. Luo, X. Sun, Y. He, Electrochim. Acta 168 (2015) 133–138.
[40] S. Reddy, R. Du, L. Kang, N. Mao, J. Zhang, Appl. Catal. B Environ. 194 (2016) 16–21.
[41] P. Xiao, Y. Yan, X. Ge, Z. Liu, J.-Y. Wang, X. Wang, Appl. Catal. B Environ. 154–155 (2014) 232–237.
[42] J. Wang, W. Cui, Q. Liu, Z. Xing, A.M. Asiri, X. Sun, Adv. Mater. 28 (2016) 215–230.
[43] T. Kennedy, E. Mullane, H. Geaney, M. Osiak, C. O' Dwyer, K.M. Ryan, Nano Lett. 14 (2014) 716–723.
[44] A. Aijaz, J. Masa, C. Rçsler, W. Xia, P. Weide, A.J.R. Botz, R.A. Fischer, W. Schuhmann, M. Muhler, Angew. Chem. Int. Ed. 55 (2016) 4087–4091.
[45] M. Wang, T. Qian, J. Zhou, C. Yan, ACS Appl. Mater. Interfaces 9 (2017) 5213–5221.
[46] S. Jin, ACS Energy Lett. 2 (2017) 1937–1938.
[47] W. Chen, H.T. Wang, Y.Z. Li, Y.Y. Liu, J. Sun, S.H. Lee, J.S. Lee, Y. Cui, ACS Cent. Sci. 1 (2015) 244–251.
[48] T.T. Liu, A.M. Asirib, X.P. Sun, Nanoscale 8 (2016) 3911–3915.
[49] L. Zhang, T. Meng, B. Mao, D. Guo, J. Qin, M. Cao, RSC Adv. 7 (2017) 50812–50821.